Collisional magnetized shock waves: One-dimensional full particle-in-cell simulations

Masaru Nakanotani [*]
Center for Space Plasma and Aeronomic Research (CSPAR), University of Alabama in Huntsville, Huntsville, Alabama 35805, USA

Renato P. Camata
Department of Physics, University of Alabama at Birmingham, Birmingham, Alabama 35294, USA

Robert R. Arslanbekov
CFD Research Corporation, Huntsville, Alabama 35806, USA

Gary P. Zank
Center for Space Plasma and Aeronomic Research (CSPAR), University of Alabama in Huntsville, Huntsville, Alabama 35805, USA and Department of Space Science, University of Alabama in Huntsville, Huntsville, Alabama 35899, USA

(Received 11 January 2022; accepted 8 April 2022; published 27 April 2022)

Although collisional electrostatic shock waves have been investigated extensively via theory, simulations, and experiments, there are comparatively few studies about collisional magnetized shock waves. We investigate collisional magnetized shocks by performing one-dimensional full particle-in-cell simulations that incorporate ion-ion, electron-electron, and ion-electron Coulomb collisions, for perpendicular and quasiparallel shock waves. The effect of Coulomb collisions is to drive a shock wave into a more laminar state. For a perpendicular shock, the magnetic overshoot becomes small because the electron pressure perpendicular to the magnetic field is isotropized and decreases due to electron-electron collisions. For the quasiparallel case, we find that ion-electron collisions severely suppress the standing whistler wave, which is present in the form of large amplitude waves in a collisionless shock wave.

DOI: 10.1103/PhysRevE.105.045209

I. INTRODUCTION

Collisional electrostatic shock waves have been investigated extensively in recent years due to advanced technologies for plasma shock experiments. It has been confirmed that collisional shock waves can form due to the head-on or oblique merging of plasma jets produced by pulsed-power-driven rail guns [1–3]. A comprehensive study of ion heating in collisional shock waves revealed that the peak ion temperature agrees well with a theoretical model for several ion species [4]. Laser-driven collisional shock waves have been measured for the first time in Rinderknecht *et al.* [5] when they observed ions streaming at speeds in excess of the shock velocity, which contributes to the heating of upstream cold plasma.

Several theoretical and simulation studies indicate that binary Coulomb collisions play an important role in the formation of collisional electrostatic shock waves. Hybrid simulations, in which ions and electrons are solved for an extended Fokker-Planck equation and electronic temperature equation, revealed that collisional electrostatic shock waves possess a precursor region due to hot ion streaming that leads to electron heating via ion-electron collisions [6,7]. This results in a shock transition scale much wider than expected from fluid theory [8]. Recently, this feature has been confirmed in full particle-in-cell (PIC) simulations [9]. Even for electrostatic collisionless shock waves, Turrell *et al.* [10] suggested ultrafast ion heating due to Coulomb collisions between two different ion species can occur.

Although several investigations about collisional electrostatic shock waves exist, our knowledge of collisional magnetized shock waves remains very limited despite the possibility that a background magnetic field may modify the shock structure. Magnetized shock waves have been studied broadly for collisionless plasma in the context of space plasma for decades [11–14], and it is thought that the shock obliquity (defined as the angle between the shock normal and the background magnetic field upstream of the shock) is a critical parameter in determining shock structure. When the shock obliquity is perpendicular (i.e., a perpendicular shock), the shock transition scale is limited to approximately the ion gyro radius for high Mach number shocks due to ions reflected by the cross shock potential [13]. On the other hand, when the shock obliquity is parallel (i.e., a parallel shock), some reflected particles can stream into the upstream plasma flow along the background magnetic field in parallel shock waves [14]. These two distinct shock obliquities can result in very different physical mechanisms being responsible for dissipation of the incoming plasma. In this paper, we address how the inclusion of a background magnetic field modifies the structure of collisional shock waves.

[*] mn0052@uah.edu

Our approach is to investigate collisional magnetized shock waves using one-dimensional (1D) full PIC simulations. A full PIC simulation is one of the best approaches to study the dissipation process and the formation of a shock wave kinetically since the velocity distribution functions of electrons and ions are solved in a self-consistent manner coupling to Maxwell's equations. In Sec. II, we describe the simulation methods and parameters. The simulation results are shown in Sec. III. We provide summary and discussion in Sec. IV.

II. METHOD: 1D FULL PIC SIMULATION

A. Coulomb collisions

We incorporate small-angle scattering due to Coulomb collisions between particles in a standard 1D full PIC code [15]. This module can be classified as a Monte Carlo method and was developed by Sentoku *et al.* [16] and Sentoku and Kemp [17]. It represents an extension for relativistic binary collisions based on a nonrelativistic collision model [18]. This approach incorporates collisions between electron-electron, ion-ion, and ion-electron pairs and randomly chooses pairs of two particles for all particles in a cell. We can estimate the scattering angle θ from the variance,

$$\langle \tan^2(\theta/2)\rangle = N_c \nu_{\alpha\beta}\Delta t, \tag{1}$$

where N_c is the number of time steps between the calculation of the collision and the next calculation, $\nu_{\alpha\beta}$ is the frequency of Coulomb collisions between particle species α and β, and Δt is the time step. Finally, we calculate the momentum of the two particles after the collision so that the total energy is conserved.

The collision frequency $\nu_{\alpha\beta}$ can be written as [17,19]

$$\nu_{\alpha\beta} = \frac{4\pi (e_\alpha e_\beta)^2 n_l L}{m_{\alpha\beta}^2 v_{\rm rel}^3}, \tag{2}$$

where $e_{\alpha(\beta)}$ is the charge for particle $\alpha(\beta)$, n_l is the smaller density of the two densities n_α and n_β, $m_{\alpha\beta} = m_\alpha m_\beta/(m_\alpha + m_\beta)$ is the reduced mass, and $v_{\rm rel}$ is the relative velocity. Here L is the Coulomb logarithm, and we use the form $L = \ln(\lambda_D m_{\alpha\beta} v_{\rm rel}^2/|e_\alpha e_\beta|)$ [17] where λ_D is the Debye length. The collision frequency can be normalized by the electron plasma frequency ω_{pe},

$$\frac{\nu_{\alpha\beta}}{\omega_{pe}} = \frac{(e'_\alpha e'_\beta)^2 n'_l}{m'^2_{\alpha\beta} v'^3_{\rm rel}} \frac{\ln\Lambda}{\Lambda}, \tag{3}$$

where $e_{\alpha(\beta)}$, n'_l, $m'_{\alpha\beta}$, and $v'_{\rm rel}$ are normalized by the elementary charge, the upstream electron density (n_0), the electron mass, and the upstream electron thermal speed, respectively. We assume a constant value for the plasma parameter $\Lambda = 4\pi n_0 \lambda_{D0}^3$ and use $L \simeq \ln\Lambda$ for simplicity. Here, λ_{D0} is the Debye length defined by the upstream plasma parameters. We can characterize small-angle Coulomb scattering in the full PIC simulation by setting a value for the plasma parameter Λ.

B. Simulation setup and parameters

We employ the injection method to produce a shock wave. A plasma is injected with a constant speed $v_{\rm inj}$ from the left boundary and reflects off a rigid wall placed at the right boundary. A shock wave forms due to the interaction of the incoming and reflected plasma and then propagates leftward. The simulation frame, therefore, corresponds to the downstream-rest frame. The background magnetic field lies in the x-z plane, defined as $\mathbf{B} = B_0(\cos\Theta_{Bn}, 0, \sin\Theta_{Bn})$ where B_0 is the magnitude of the background magnetic field and Θ_{Bn} is the shock obliquity.

We use an ionic charge state $Z = 1$ and a reduced mass ratio, $m_i/m_e = 400$ where $m_{i(e)}$ is the ion (electron) mass. We use the following dimensionless parameters to determine the magnitude of the background magnetic field B_0, upstream ion and electron temperature, and Coulomb collision frequency, respectively: $\Omega_{ce}/\omega_{pe} = 0.1$, $\beta_i = \beta_e = 0.5$, and $\Lambda = 175$. Here, $\Omega_{ce} = eB_0/m_e c$ is the electron cyclotron frequency and $\beta_{i(e)} = 8\pi k_B T_{i(e)}/B_0^2$ the ion (electron) plasma beta. With this choice of Λ, the ion-electron collision to the electron plasma frequency ratio, for instance, becomes $\nu_{ie}/\omega_{pe} \sim 0.03$, $\nu_{ie}/\Omega_{ce} \sim 0.3$ by assuming $v'_{\rm rel} \sim 1$. In the same way, the ion-ion collision frequency is $\nu_{ii}/\omega_{pi} \sim 0.12$ and $\nu_{ii}/\Omega_{ci} \sim 24$ using the ion thermal speed as the relative speed. These parameters are defined using upstream plasma parameters. We use 500 particles per cell. The injection speed is $v_{\rm inj} = 0.02c$ where c is the speed of light in vacuum and the corresponding Alfvén Mach number is $M_{A,{\rm inj}} = 4$. The grid size is $\Delta x = 0.05\lambda_e$, where $\lambda_e = c/\omega_{pe}$ is the electron skin depth, and the time step is $\Delta t = 0.05\omega_{pe}^{-1}$. To reduce the computational cost, we choose $N_c = 10$. We consider two cases to discuss the effect of shock obliquities on collisional magnetized shock waves: (i) a perpendicular shock wave, $\Theta_{Bn} = 90^\circ$, and (ii) a quasiparallel shock wave, $\Theta_{Bn} = 30^\circ$. We use a different simulation size, $L_x = 500\lambda_e$ and $1000\lambda_e$, for the perpendicular and quasiparallel case, respectively. Here, we choose these physical parameters so that we can compare collisional shock waves with collisionless shock waves which have been investigated in detail.

III. RESULTS

A. Perpendicular shock: $\Theta_{Bn} = 90^\circ$

Figure 1 shows the spatiotemporal evolution of the component of the magnetic field B_z together with cuts of B_z and the electrostatic potential Φ at $T = 8.6\Omega_{ci}^{-1}$, from top to bottom. The left and right panels correspond to the collisionless and collisional cases, respectively. For the collisionless case, the shock speed is estimated as $v_{\rm sh} \sim 0.0125c$. A strong overshoot ($B_z \sim 6B_0$) has developed by $T = 7$ and $8.6\Omega_{ci}^{-1}$ as illustrated in the top-left panel. This is the typical structure for supercritical perpendicular shock waves [20–23]. Considering in B_z, the scales of the foot (the region between the first two vertical dashed lines) and ramp (the region between the second and third vertical dashed lines) regions are $33\lambda_e$ and $9\lambda_e$, respectively. The maximum strength of the magnetic field is $\sim 6B_0$ and there are other clear overshoots at $X = 320\lambda_e$ and $450\lambda_e$ and undershoots at $X = 280\lambda_e$ and $390\lambda_e$. The electrostatic field at the shock front is roughly estimated as $E_x/B_0 \sim \frac{\phi_{\rm max}-\phi_{\rm min}}{\Delta L} \sim 0.003\,38$ where $\phi_{\rm max} \sim 0.135$, $\phi_{\rm min} \sim 0$, and $\Delta L = 40\lambda_e$ (the distance between the two dashed lines). The shock-jump condition for the magnetic field component B_z derived from the Rankine-Hugoniot condition yields a

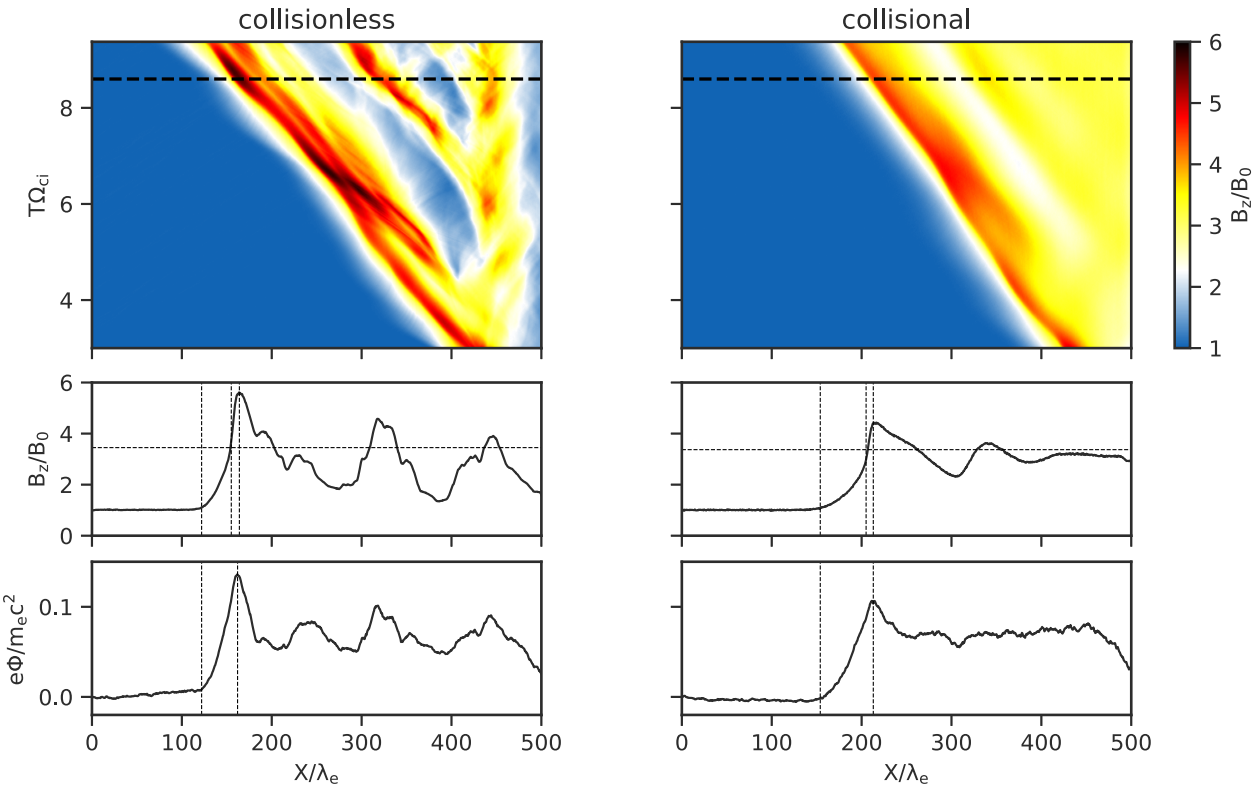

FIG. 1. From top to bottom, the spatiotemporal evolution of B_z, the profile of B_z, and the electrostatic potential at $T = 8.6\Omega_{ci}^{-1}$ from top to bottom for the collisionless (left) and collisional (right) cases.

value of 3.45 (the horizontal dashed line in the middle panel). The simulated profile deviates from the jump condition due to the overshoots and undershoots.

Coulomb collisions play a role in rendering a shock wave laminar. For the collisional case, the shock speed is $0.01c$, which is slightly slower than the collisionless shock wave. From the top-right panel of Fig. 1, it is clear that the shock is quite stationary and laminar in the spatiotemporal plot. The profiles of B_z and Φ are cuts taken at the same time $T = 8.6\Omega_{ei}^{-1}$, and it is clear that the overshoots and undershoots are less significant. The downstream magnetic field is almost constant at $3B_0$. The maximum magnitude of B_z is around $4B_0$, and the foot and ramp scales are $51\lambda_e$ and $8\lambda_e$, respectively. The electrostatic potential corresponds to a weaker electrostatic field at the shock front with $E_x/B_0 \sim 0.001\,78$ where $\phi_{\max} \sim 0.105$, $\phi_{\min} \sim 0$, and $\Delta L = 59\lambda_e$. The weaker E_x reduces the number of reflected ions. The shock-jump condition for the magnetic field component B_z derived from the Rankine-Hugoniot condition is 3.37 (the horizontal dashed line in the middle panel). The simulated profile becomes closer to the jump condition since Coulomb collisions tend to suppress overshoots and undershoots. It is worth mentioning that the mean free path of ion-ion collisions becomes $\sim 232\lambda_e$ upstream using the injection speed as the relative speed in Eq. (3). This is much larger than the shock transition scale.

Figure 2 shows the ion phase space for the three velocity components v_x, v_y, and v_z from top to bottom for the collisionless (left panels) and collisional (right panels) cases at $T = 8.6\Omega_{ci}^{-1}$. For both cases, we observe that some ions are reflected at the shock front. The downstream state of the collisional shock is more thermalized than that of the collisionless shock thanks to collisional effects rapidly equilibrating the plasma. The $X - v_z$ space of the collisionless case shows no significant change across the shock wave because the shock angle is strictly perpendicular, and the plasma motions parallel and perpendicular to the background magnetic field are completely decoupled. On the other hand, it can be seen from the $X - v_z$ space of the collisional shock that the plasma is heated parallel to the magnetic field in both the foot region and the downstream region due to Coulomb collisions. Electrons are also heated parallel to the magnetic field thanks to ion-electron collisions (not shown here).

The absence of a strong overshoot in the collisional case is a consequence of a decrease in the electrostatic shock potential. As mentioned in [24], the magnetic overshoot at the shock front is thought to be the region where most of the incoming ions are stopped and reflected. Therefore, if there is a strong electrostatic potential (or field) at the shock front that acts to strongly decelerate incoming ions, the magnitude of an overshoot can become large. The electrostatic potential in a shock wave can be written in the following form by assuming a massless electron fluid [25,26]:

$$e\Phi(X) = e\int_{-\infty}^{X} \frac{1}{c} V_{ey} B_z dx + \int_{-\infty}^{X} \frac{1}{n} \frac{\partial P_{e\perp}}{\partial x} dx, \qquad (4)$$

where V_{ey} is the y component of the electron mean velocity and $P_{e\perp}$ is the electron pressure perpendicular to the magnetic field. The top panel of Fig. 3 shows a potential calculated using Eq. (4) with simulated values. We plot the first and second terms for both the collisionless and collisional cases,

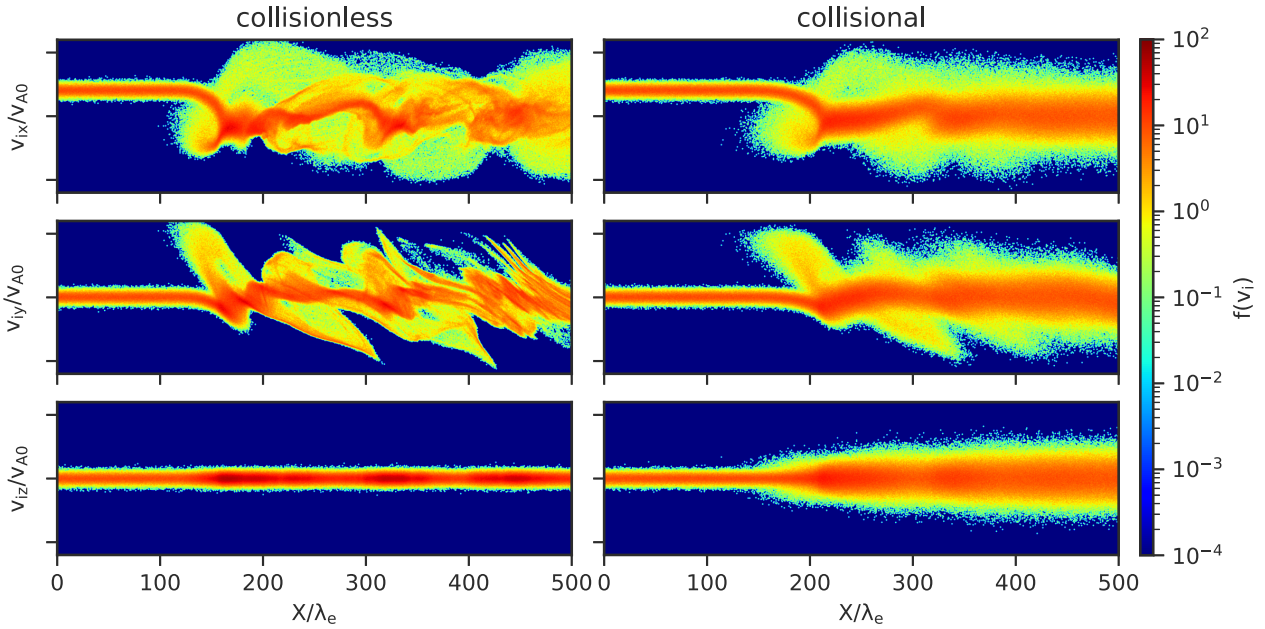

FIG. 2. From top to bottom, the ion phase space density for three velocities v_x, v_y, and v_z for the collisionless (left) and collisional (right) case at $T = 8.6\Omega_{ci}^{-1}$.

separately. The second term (the gradient of the electron pressure perpendicular to the magnetic field) of the collisional shock is smaller than that of the collisionless shock while the first terms have the same value at the overshoot ($X \sim 150\lambda_e$). This illustrates that the change in the potential is due to the decrease of the electron perpendicular pressure in the collisional case compared with that of the collisionless case. This is further supported in the bottom panel of Fig. 3 that shows the electron parallel (black) and perpendicular (orange) pressures for the collisionless (dashed line) and collisional (solid line) shocks. The difference in the electron perpendicular pressure is caused by electron-electron collisions that isotropize the electron parallel and perpendicular pressures, which were initially anisotropic because reflected ions preferentially heat electrons in the perpendicular direction. This can be confirmed from the dashed lines in the bottom panel. Therefore, in the collisional shock, the perpendicular electron pressure is isotropized, and then the gradient of the pressure decreases. This leads to a decrease of the electrostatic potential and hence the suppression of a strong overshoot.

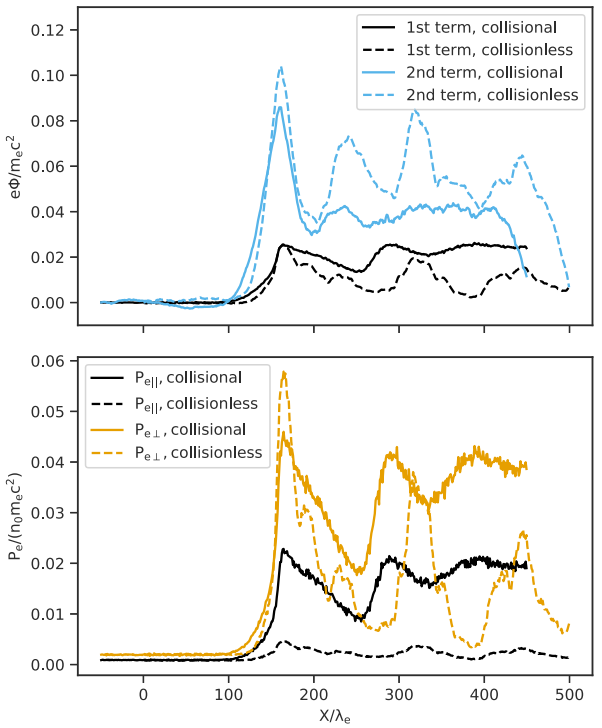

FIG. 3. Top panel: electrostatic potential calculated according to Eq. (4). Bottom panel: electron parallel and perpendicular pressures.

B. Quasiparallel shock: $\Theta_{Bn} = 30°$

Figure 4 displays the spatiotemporal evolution of the fluctuating B_z, i.e., the departure of the z component of the magnetic field from the background magnetic field $B_{z0} = B_0 \sin\Theta_{Bn}$ (top panel) and magnetic field components B_y and B_z at $T = 11\Omega_{ci}^{-1}$ (bottom panel) for a collisionless (left) and collisional (right) shock case. For the collisionless case, the location of the shock wave is around $X = 800\lambda_e$ at $T = 11\Omega_{ci}^{-1}$. Large-amplitude waves are excited in front of the collisionless quasiparallel shock wave and extend upstream until $X = 200\lambda_e$ at $T = 11\Omega_{ci}^{-1}$. The amplitude roughly ranges from $1B_0$ to $3B_0$, and the waves are excited in both B_y and B_z (the bottom panel).. Figure 5 shows the hodogram of B_y and B_z from $X = 300\lambda_e$ to $400\lambda_e$ at $T = 11\Omega_{ci}^{-1}$, and confirms that the excited waves are circularly and right-handed polarized. The density profile upstream of the shock wave is approximately constant, indicating that the waves are incompressible (not shown here). The wavelength is $\lambda_w \sim 30\lambda_e$ and corresponds to a wave number $k_w = 2\pi/\lambda_w \sim 0.21\lambda_e^{-1}$. Since the

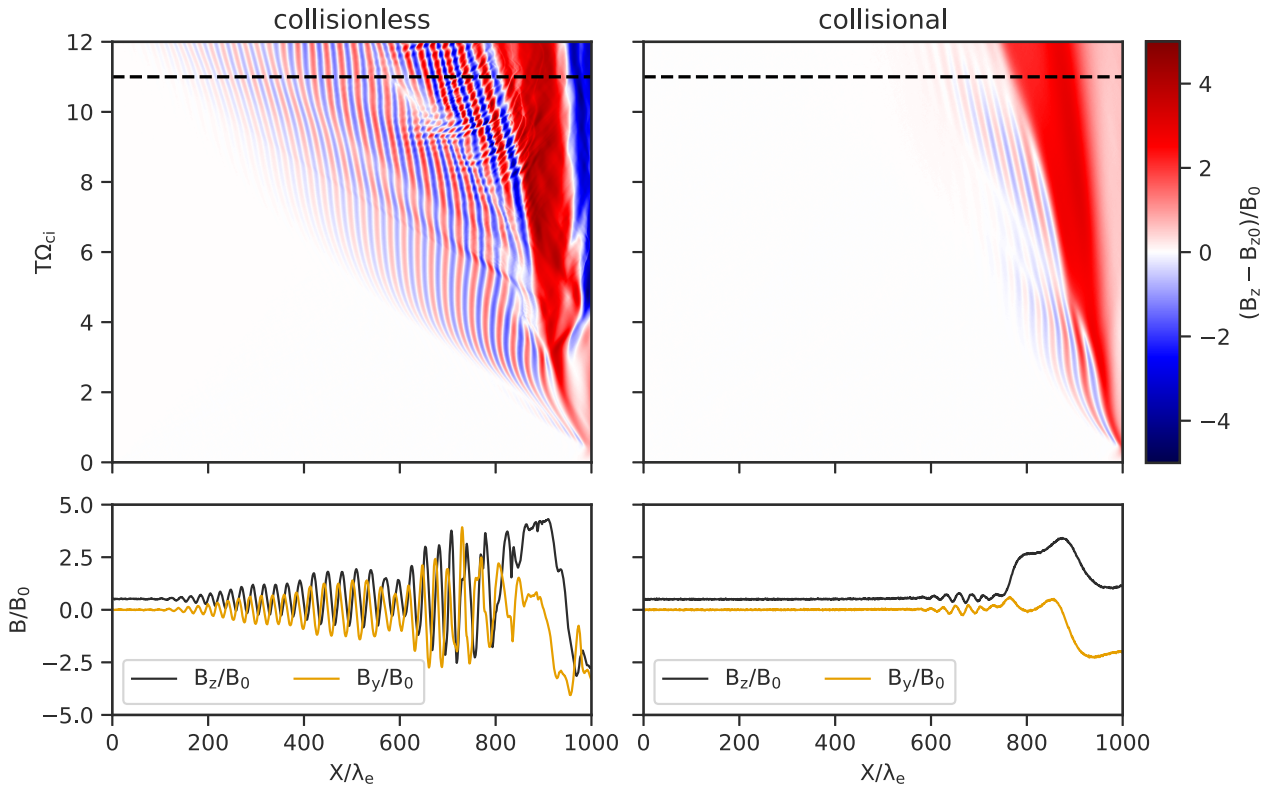

FIG. 4. Spatiotemporal evolution of B_z (top) and the cut of B_z at $T = 11\Omega_{ci}^{-1}$ (bottom) for the collisionless (left) and collisional (right) cases.

phase speed of the excited waves corresponds to about 0 in the simulation frame, it gives $\omega/k_w \sim 0.02c$ in the shock-rest frame by estimating the shock speed as 0.02.

The large-amplitude waves are whistler waves that phase-stand ahead of the shock wave. The dispersion relation for low-frequency whistler waves in the cold-plasma limit is [27]

$$2R = 1 + (1+z^2)\cos^2\Theta_{Bn} + \sqrt{\{1+(1+z^2)\cos^2\Theta_{Bn}\}^2 - 4\cos^2\Theta_{Bn}}, \quad (5)$$

where $R = \omega^2/(kv_{A0}^2)$ and $z = k^2c^2/\omega_{pi}^2$ with v_{A0} representing the upstream Alfvén speed and ω_{pi} the upstream ion plasma frequency. The simulated wave number and frequency satisfy the condition (5). A condition for the presence of precursor whistler waves is given by $M_A < M_w$ [28] where

$$M_w = \frac{|\cos\Theta_{Bn}|}{2\mu^{1/2}}. \quad (6)$$

Here, $\mu = m_e/m_i$. Using the simulation parameters, we see that $M_w \sim 8.7$, meaning that the condition for precursor whistler waves is satisfied in our simulation. Moreover, the theoretical wave number for phase-standing whistler waves is given by [29,30]

$$k_w \simeq \mu^{1/2}\frac{(M_A^2-1)^{1/2}}{\cos\Theta_{Bn}}\frac{\omega_{pe}}{c}. \quad (7)$$

Substituting the simulation parameters into the above equation, we obtain $k_w \sim 0.22$, which agrees well with the wave number obtained in the simulation. Therefore, we conclude that the observed waves are whistler waves.

For the collisional case, the excitation of whistler waves upstream of the shock is severely suppressed. The

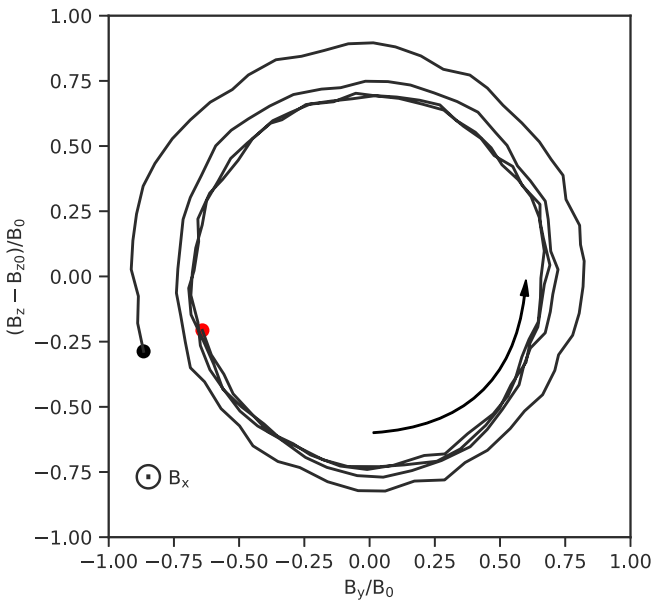

FIG. 5. Hodogram of B_y and B_z from $X = 200\lambda_e$ (red point) to $400\lambda_e$ (black point) at $T = 11\Omega_{ci}^{-1}$.

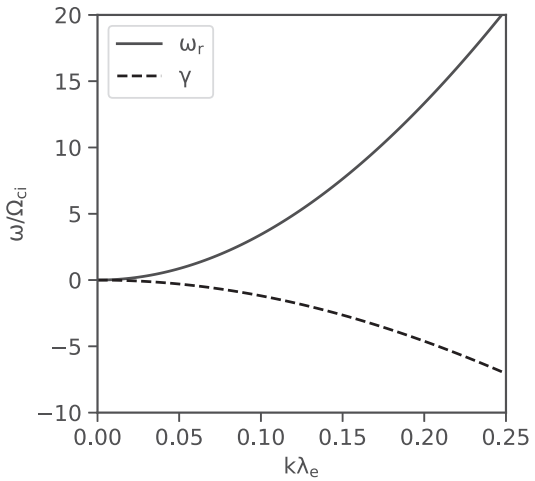

FIG. 6. Dispersion relation of the whistler mode with a collisional effect [the solution of Eq. (8)]. The real and imaginary parts of the wave frequency are ω_r and γ, respectively.

spatiotemporal evolution of B_z (the right panel, Fig. 4) shows that the shock evolution is similar to the collisionless case. However, no evident wave excitation is seen upstream. Although some waves can be observed at $T = 4\Omega_{ci}^{-1}$ and $8\Omega_{ci}^{-1}$, they are found only in the vicinity of the shock and the amplitude is much smaller than the collisionless case. We can confirm that the y component of the waves is also small in the bottom panel. As described above, the downstream state of a collisional shock wave is considerably laminar more than the collisionless parallel case.

The suppression of the whistler waves is likely due to the collisional damping of the whistler mode. The dispersion relation of the whistler mode when Coulomb ion-electron collisions are included is given by [31–33]

$$\frac{c^2k^2}{\omega^2} = 1 - \frac{\omega_{pe}^2}{\omega(\omega + i\nu_{ie} - \Omega_{ce}\cos\Theta_{Bn})}. \tag{8}$$

Solutions of the lower-frequency whistler mode dispersion relation (8) using the simulation parameters are plotted in Fig. 6. Here, the frequency $\omega = \omega_r + i\gamma$ with ω_r (γ) the real (imaginary) part. Since the simulated wavelength of whistler waves in the collisionless case is $k_w = 0.21$, this gives a damping rate $\gamma \sim -5\Omega_{ci}$. This corresponds to an imaginary to real frequency ratio $\gamma/\omega_r \sim 0.3$. Comparing other possible damping mechanisms [34], such as Landau and cyclotron damping, the obtained ratio is much stronger than the other mechanisms and is the fastest mechanism to suppress whistler waves.

As discussed in several previous studies [27,35–37], precursor whistler waves contribute to the dissipation of an incoming plasma at a shock wave. From top to bottom, Fig. 7 shows ion phase spaces for the three velocities v_x, v_y, and v_z in the collisionless case (left) and collisional case (right). We can see an apparent ion beam from $X = 0$–$400\lambda_e$ in the collisionless case. Furthermore, several ion holes form over $X = 400\lambda_e$–$600\lambda_e$ due to ion trapping by the whistler waves [27]. In the region $X = 600\lambda_e$–$800\lambda_e$, the amplitude of the waves becomes strong enough to dissipate the core ion, and then the plasma develops into a downstream state. Excited whistler waves play an important role in dissipating the incoming plasma.

On the other hand, in the collisional case, Coulomb collisions are a dominant process and thermalize the ion beam rather than excited whistler waves. In the right panels of Fig. 7, we can confirm that some ions stream upstream against the incoming plasma even though they are thermalized due to Coulomb collisions between ions and electrons. We also see that ion holes are completely absent in the collisional case.

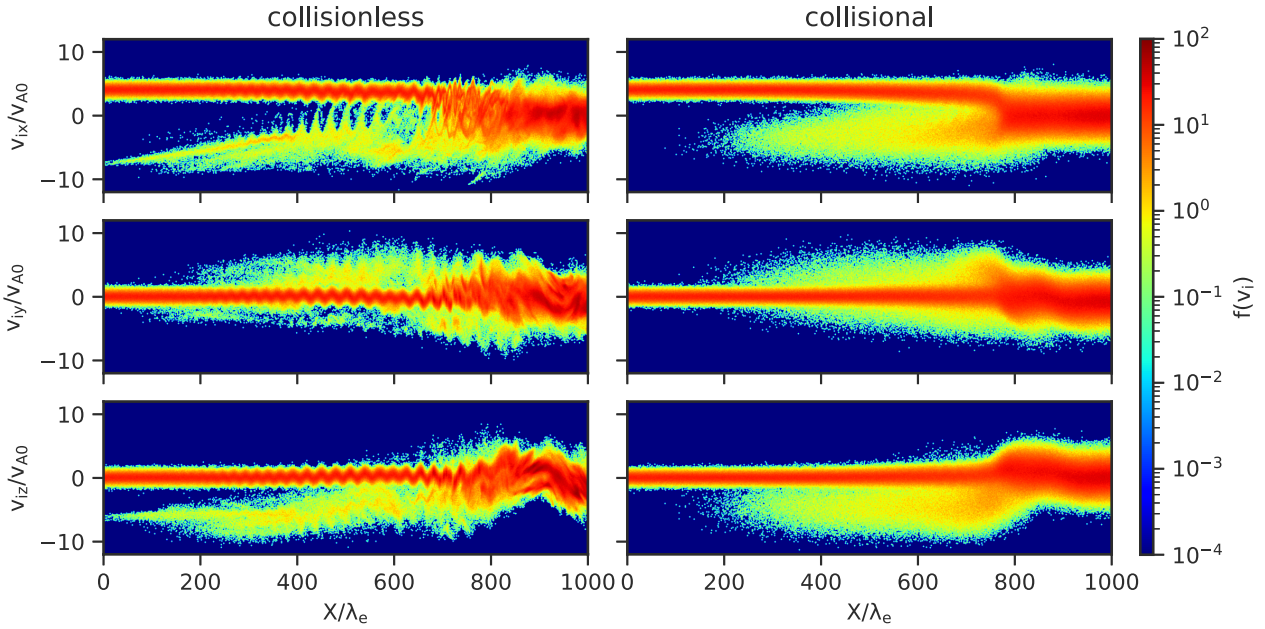

FIG. 7. Ion phase space density for three velocities (v_x, v_y, and v_z from top to bottom) for the collisionless (left) and collisional (right) case at $T = 11\Omega_{ci}^{-1}$.

IV. SUMMARY AND DISCUSSION

We have investigated collisional magnetized shock waves using 1D full PIC simulations and incorporated small-angle scattering due to ion-ion, ion-electron, and electron-electron Coulomb collisions. We considered two cases: (i) a perpendicular shock ($\Theta_{Bn} = 90^\circ$) and (ii) a quasiparallel shock ($\Theta_{Bn} = 30^\circ$). The Alfvén Mach number in the shock rest frame is $M_A \sim 6$ and 4.8 for the perpendicular and quasiparallel shock case, respectively. Common parameters are the ion and electron plasma beta $\beta_i = \beta_e = 0.5$, $\omega_{pe}/\Omega_{ce} = 10$, and for the Coulomb collisions, we choose the plasma parameter $\Lambda = 175$, which gives, for example, the ratio $\nu_{ie}/\omega_{pe} \sim 0.03$.

For the perpendicular shock case, we find that a collisional shock wave tends to be more laminar, unlike a collisionless shock wave. Overshoots and undershoots observed in the collisional shock are less significant, and the maximum value of B_z at the shock front is 0.4 (0.6 for the collisionless shock). No cyclic behavior with a strong overshoot is seen in the collisional shock. This is because anisotropy between the electron parallel and perpendicular pressure ($P_{e\parallel} < P_{e\perp}$) is isotropized by electron-electron collisions, causing a potential drop according to Eq. (4).

For the quasiparallel shock case, the most important finding is that ion-electron Coulomb collisions suppress the whistler wave excitation. In a collisionless quasiparallel shock, large amplitude whistler waves are observed ahead of the shock wave. These waves trap the ion beam and are eventually dissipated by the core ions. On the other hand, Coulomb collisions thermalize the ion beam in the collisional shock and ion trapping by whistler waves is unnecessary. The suppression of whistler waves in the collisional case is due to collisional wave damping.

Let us consider a parameter dependence on a collisional perpendicular shock wave. As pointed out by Scholer *et al.* [23], when the ion beta becomes low ($\beta_i \leqslant 0.4$), cyclic reformation at the shock front is noticeably present and occurs with a timescale of $1 - 2\Omega_{ci}^{-1}$. If Coulomb collisions were strong enough to thermalize reflected ions during the reformation process, the reformation process might be expected to be suppressed, with the result that the shock structure becomes stationary and laminar. It may be helpful to compare the "slowing-down" collisional timescale [18] to the reformation timescale to see whether such suppression occurs.

Coulomb collisions might have a significant effect at particle acceleration on quasiparallel shock waves. Wave excitation, especially upstream of a parallel shock wave, is critical to enable pitch-angle scattering of particles for producing energetic particles in the context of the diffusive shock acceleration (DSA) [38–42]. Nicolas [43] shows that Coulomb collisions between ions can suppress the magnetic streaming instability induced by an ion beam since collisions provide the heating of the ion beam. Moreover, as we showed in the collisional shock with $\Theta_{Bn} = 30^\circ$, Coulomb collisions suppressed whistler wave excitation by collisional wave damping. These waves may contribute to accelerate particles to be injected into the DSA process [44,45]. In this case, particles are unlikely to be energized, and we can expect that particles will not be accelerated to very high energies in a collisional shock wave. This may have important implications for the acceleration of cosmic rays by supernova remnant shock waves in a collisional interstellar medium.

The rippling of collisionless shock waves, which is seen in multidimensional simulations, is expected to be suppressed when effects of Coulomb collisions are significant. The shock rippling can be the consequence of the Alfvén ion cyclotron (AIC) instability driven by temperature anisotropy at the shock front [46]. However, if Coulomb collisions isotropize the temperature anisotropy at the shock transition region faster than the growth rate of the AIC instability, shock rippling is suppressed, and one-dimensional simulations can be valid for a wide range of shock parameters. Since it has been pointed out that the presence of ripplings may change the efficiency of particle acceleration [47], Coulomb collisions introduce the possibility of modifying the efficiency from this perspective.

Collisional effects may also mediate low Mach number (subcritical) shock waves. In this paper, we only consider supercritical shock waves in which reflected ions play an important role to provide an additional dissipation. However, since reflected ions are not significant in subcritical shock waves, the dissipation process in the transition region is only due to microinstabilities for collisionless shock waves [11]. If collisional effects are significant, it is possible that collisions suppress the onset of microinstabilities. In this case, the length scale of the shock transition region can be determined by the collisional length scale and results in a broader transition region [48]. We also expect that the effect of the background magnetic field can be ignored when a collision frequency is much faster than the gyrofrequency since the gyro motions are scattered by collisions. It is possible to verify this by using an artificially high collisionality in the full PIC simulation.

Finally, we comment on a point related to the scaling behavior of the collision frequency. Since the ion-electron collision frequency, for instance, scales as $\nu_{ie} \propto Z^2$ where Z is the ion charge state, ion-electron collisions can be important for the structure of a shock wave when multicharged ions are considered. On the other hand, the ion-ion collision frequency for heavy ions scales as $\nu_{ii} \propto Z^4/\Gamma^2$ where Γ is the ratio of the ion mass to the proton mass. Therefore, the collision frequency can be low for large Γ. This situation is often encountered in laser-shock experiments [49–53]. In this case, reflected ions from a shock front can be thermalized on the ion cyclotron timescale and might be expected to form a precursor region as discussed for electrostatic collisional shock waves [9]. Note that this structure still forms without ion-ion collisions [9].

ACKNOWLEDGMENTS

We acknowledge the partial support of an NSF EPSCoR RII-Track-1 Cooperative Agreement, OIA-1655280. M.N. and G.P.Z. acknowledge partial support from a NASA IMAP subaward under NASA Contract No. 80GSFC19C0027. This work was made possible in part by the provision of high performance computing resources and technical support from the Alabama Supercomputer Authority.

[1] E. C. Merritt, A. L. Moser, S. C. Hsu, J. Loverich, and M. Gilmore, Experimental Characterization of the Stagnation Layer between Two Obliquely Merging Supersonic Plasma Jets, Phys. Rev. Lett. **111**, 085003 (2013).

[2] E. C. Merritt, A. L. Moser, S. C. Hsu, C. S. Adams, J. P. Dunn, A. Miguel Holgado, and M. A. Gilmore, Experimental evidence for collisional shock formation via two obliquely merging supersonic plasma jets, Phys. Plasmas **21**, 055703 (2014).

[3] A. L. Moser and S. C. Hsu, Experimental characterization of a transition from collisionless to collisional interaction between head-on-merging supersonic plasma jets, Phys. Plasmas **22**, 055707 (2015).

[4] S. J. Langendorf, K. C. Yates, S. C. Hsu, C. Thoma, and M. Gilmore, Experimental Measurements of Ion Heating in Collisional Plasma Shocks and Interpenetrating Supersonic Plasma Flows, Phys. Rev. Lett. **121**, 185001 (2018).

[5] H. G. Rinderknecht, H. S. Park, J. S. Ross, P. A. Amendt, D. P. Higginson, S. C. Wilks, D. Haberberger, J. Katz, D. H. Froula, N. M. Hoffman *et al.*, Highly Resolved Measurements of a Developing Strong Collisional Plasma Shock, Phys. Rev. Lett. **120**, 095001 (2018).

[6] M. Casanova, O. Larroche, and J.-P. Matte, Kinetic Simulation of a Collisional Shock Wave in a Plasma, Phys. Rev. Lett. **67**, 2143 (1991).

[7] F. Vidal, J. P. Matte, M. Casanova, and O. Larroche, Ion kinetic simulations of the formation and propagation of a planar collisional shock wave in a plasma, Phys. Fluids B **5**, 3182 (1993).

[8] S. I. Braginskii, Transport processes in a plasma, Rev. Plasma Phys. **1**, 205 (1965).

[9] W. S. Zhang, H. B. Cai, B. Du, D. G. Kang, S. Y. Zou, and S. P. Zhu, Full particle-in-cell simulation of the formation and structure of a collisional plasma shock wave, Phys. Rev. E **103**, 023213 (2021).

[10] A. E. Turrell, M. Sherlock, and S. J. Rose, Ultrafast collisional ion heating by electrostatic shocks, Nat. Commun. **6**, 8905 (2015).

[11] C. S. Wu, Physical mechanisms for turbulent dissipation in collisionless shock waves, Space Sci. Rev. **32**, 83 (1982).

[12] C. F. Kennel, J. P. Edmiston, and T. Hada, A quarter century of collisionless shock research, *Collisionless Shocks in the Heliosphere: A Tutorial Review* (American Geophysical Union, 1985), pp. 1–36.

[13] B. Lembege, J. Giacalone, M. Scholer, T. Hada, M. Hoshino, V. Krasnoselskikh, H. Kucharek, P. Savoini, and T. Terasawa, Selected problems in collisionless-shock physics, Space Sci. Rev. **110**, 161 (2004).

[14] D. Burgess and M. Scholer, Microphysics of quasi-parallel shocks in collisionless plasmas, Space Sci. Rev. **178**, 513 (2013).

[15] C. K. Birdsall and A. B. Langdon, *Plasma Physics via Computer Simulation* (CRC Press, 1991).

[16] Y. Sentoku, K. Mima, Y. Kishimoto, and M. Honda, Effects of relativistic binary collisions on PIC simulation of laser plasmas, J. Phys. Soc. Jpn. **67**, 4084 (1998).

[17] Y. Sentoku and A. J. Kemp, Numerical methods for particle simulations at extreme densities and temperatures: Weighted particles, relativistic collisions and reduced currents, J. Comput. Phys. **227**, 6846 (2008).

[18] T. Takizuka and H. Abe, A binary collision model for plasma simulation with a particle code, J. Comput. Phys. **25**, 205 (1977).

[19] L. Spitzer, *Physics of Fully Ionized Gases* (Courier Corporation, 1956).

[20] D. Biskamp and H. Welter, Structure of the Earth's bow shock, J. Geophys. Res. **77**, 6052 (1972).

[21] D. Biskamp, Collisionless shock waves in plasmas, Nucl. Fusion **13**, 719 (1973).

[22] B. Lembege and J. M. Dawson, Self-consistent study of a perpendicular collisionless and nonresistive shock, Phys. Fluids **30**, 1767 (1987).

[23] M. Scholer, I. Shinohara, and S. Matsukiyo, Quasi-perpendicular shocks: Length scale of the cross-shock potential, shock reformation, and implication for shock surfing, J. Geophys. Res.: Space Phys. **108**, 1014 (2003).

[24] A. Balogh and R. A. Treumann, *Physics of Collisionless Shocks* (Springer Science & Business Media, 2013), Vol. 12.

[25] M. M. Leroy, C. C. Goodrich, D. Winske, C. S. Wu, and K. Papadopoulos, Simulation of a perpendicular bow shock, Geophys. Res. Lett. **8**, 1269 (1981).

[26] M. M. Leroy, D. Winske, C. C. Goodrich, C. S. Wu, and K. Papadopoulos, The structure of perpendicular bow shocks, J. Geophys. Res. **87**, 5081 (1982).

[27] F. G. E. Pantellini, A. Heron, J. C. Adam, and A. Mangeney, The role of the whistler precursor during the cyclic reformation of a quasi-parallel shock, J. Geophys. Res. **97**, 1303 (1992).

[28] V. V. Krasnoselskikh, B. Lembège, P. Savoini, and V. V. Lobzin, Nonstationarity of strong collisionless quasiperpendicular shocks: Theory and full particle numerical simulations, Phys. Plasmas **9**, 1192 (2002).

[29] D. A. Tidman and N. A. Krall, *Shock Waves in Collisionless Plasmas* (Wiley, New York, 1971).

[30] M. Scholer and D. Burgess, Whistler waves, core ion heating, and nonstationarity in oblique collisionless shocks, Phys. Plasmas **14**, 072103 (2007).

[31] T. H. Stix, *Waves in Plasmas* (Springer Science & Business Media, 1992).

[32] Y. Mouzouris and J. E. Scharer, Wave propagation and absorption simulations for helicon sources, Phys. Plasmas **5**, 4253 (1998).

[33] W. Li, B. Zhao, G. Wang, and D. Xiang, Landau and collisional damping induced power deposition for the $m = 0$ mode of helicon and Trivelpiece-Gould waves in high density helicon plasmas, AIP Adv. **10**, 085008 (2020).

[34] S. P. Gary and M. M. Mellott, Whistler damping at oblique propagation: Laminar shock precursors, J. Geophys. Res. **90**, 99 (1985).

[35] N. Omidi, K. B. Quest, and D. Winske, Low Mach number parallel and quasi-parallel shocks, J. Geophys. Res. **95**, 20717 (1990).

[36] J. R. Kan, M. E. Mandt, and L. H. Lyu, Quasi-parallel collisionless shocks, Space Sci. Rev. **57**, 201 (1991).

[37] M. Scholer, H. Kucharek, and I. Shinohara, Short large-amplitude magnetic structures and whistler wave precursors in a full-particle quasi-parallel shock simulation, J. Geophys. Res.: Space Phys. **108**, 1273 (2003).

[38] W. I. Axford, E. Leer, and G. Skadron, The acceleration of cosmic rays by shock waves, in *International Cosmic Ray Conference* (Springer, 1977), Vol. 11, p. 132.

[39] R. D. Blandford and J. P. Ostriker, Particle acceleration by astrophysical shocks, Astrophys. J., Lett. **221**, L29 (1978).

[40] A. R. Bell, The acceleration of cosmic rays in shock fronts—I., Mon. Not. R. Astron. Soc. **182**, 147 (1978).

[41] R. Blandford and D. Eichler, Particle acceleration at astrophysical shocks: A theory of cosmic ray origin, Phys. Rep. **154**, 1 (1987).

[42] W. K. M. Rice, G. P. Zank, and G. Li, Particle acceleration and coronal mass ejection driven shocks: Shocks of arbitrary strength, J. Geophys. Res.: Space Phys. **108**, 1369 (2003).

[43] L. Nicolas, Effects of collisions on the magnetic streaming instability, Ph.D. thesis, Université Pierre et Marie Curie - Paris VI, 2017.

[44] Y. Kuramitsu and V. Krasnoselskikh, Gyroresonant Surfing Acceleration, Phys. Rev. Lett. **94**, 031102 (2005).

[45] T. Terasawa and S. Matsukiyo, Cyclotron resonant interactions in cosmic particle accelerators, Space Sci. Rev. **173**, 623 (2012).

[46] D. Burgess and M. Scholer, Shock front instability associated with reflected ions at the perpendicular shock, Phys. Plasmas **14**, 012108 (2007).

[47] S. Matsukiyo and Y. Matsumoto, Electron acceleration at a high beta and low Mach number rippled shock, J. Phys.: Conf. Ser. **642**, 012017 (2015).

[48] P. Mostafavi and G. P. Zank, The structure of shocks in the very local interstellar medium, Astrophys. J., Lett. **854**, L15 (2018).

[49] L. Romagnani, S. V. Bulanov, M. Borghesi, P. Audebert, J. C. Gauthier, K. Löwenbrück, A. J. Mackinnon, P. Patel, G. Pretzler, T. Toncian, and O. Willi, Observation of Collisionless Shocks in Laser-Plasma Experiments, Phys. Rev. Lett. **101**, 025004 (2008).

[50] Y. Kuramitsu, Y. Sakawa, T. Morita, C. D. Gregory, J. N. Waugh, S. Dono, H. Aoki, H. Tanji, M. Koenig, N. Woolsey, and H. Takabe, Time Evolution of Collisionless Shock in Counterstreaming Laser-Produced Plasmas, Phys. Rev. Lett. **106**, 175002 (2011).

[51] H.-S. Park, D. D. Ryutov, J. S. Ross, N. L. Kugland, S. H. Glenzer, C. Plechaty, S. M. Pollaine, B. A. Remington, A. Spitkovsky, L. Gargate *et al.*, Studying astrophysical collisionless shocks with counterstreaming plasmas from high power lasers, High Energy Density Phys. **8**, 38 (2012).

[52] H. Ahmed, M. E. Dieckmann, L. Romagnani, D. Doria, G. Sarri, M. Cerchez, E. Ianni, I. Kourakis, A. L. Giesecke, M. Notley *et al.*, Time-Resolved Characterization of the Formation of a Collisionless Shock, Phys. Rev. Lett. **110**, 205001 (2013).

[53] T. Umeda, R. Yamazaki, Y. Ohira, N. Ishizaka, S. Kakuchi, Y. Kuramitsu, S. Matsukiyo, I. Miyata, T. Morita, Y. Sakawa *et al.*, Full particle-in-cell simulation of the interaction between two plasmas for laboratory experiments on the generation of magnetized collisionless shocks with high-power lasers, Phys. Plasmas **26**, 032303 (2019).